Tunable Ultrasmall Visible-to-Extended Near-Infrared Emitting Silver Sulfide Quantum Dots for Integrin-Targeted Cancer Imaging

Rui Tang, Jianpeng Xue, Baogang Xu, Duanwen Shen, Gail P. Sudlow, and Samuel Achilefu*

Department of Radiology, Washington University in St. Louis, School of Medicine, St. Louis, Missouri 63110, United States

ABSTRACT The large size of many near-infrared (NIR) fluorescent nanoparticles prevents rapid extravasation from blood vessels and subsequent diffusion to tumors. This confines *in vivo* uptake to the peritumoral space and results in high liver retention. In this study, we developed a viscosity modulated approach to synthesize ultrasmall silver sulfide quantum dots (QDs) with distinct tunable light emission from 500 to 1200 nm and a QD core diameter between 1.5 and 9 nm. Conjugation of a tumor-avid cyclic pentapeptide (Arg-Gly-Asp-DPhe-Lys) resulted in monodisperse, water-soluble QDs (hydrodynamic diameter < 10 nm) without loss of the peptide's high binding affinity to tumor-associated integrins (K_I = 1.8 nM/peptide). Fluorescence and electron microscopy showed that selective integrin-mediated internalization was observed only in cancer cells treated with the peptide-labeled QDs, demonstrating that the unlabeled hydrophilic nanoparticles exhibit characteristics of negatively charged fluorescent dye molecules, which typically do not internalize in cells. The biodistribution profiles of intravenously administered QDs in different mouse models of cancer reveal an exceptionally high tumor-to-liver uptake ratio, suggesting that the small sized QDs evaded conventional opsonization and subsequent high uptake in the liver and spleen. The seamless tunability of the QDs over a wide spectral range with only a small increase in size, as well as the ease of labeling the bright and noncytotoxic QDs with biomolecules, provides a platform for multiplexing information, tracking the trafficking of single molecules in cells, and selectively targeting disease biomarkers in living organisms without premature QD opsonization in circulating blood.

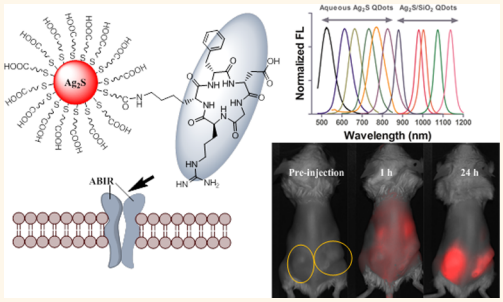

KEYWORDS: silver sulfide · near-infrared · tumor · microscopy · small animal · optical imaging

Fluorescent nanoparticles, especially quantum dots (QDs), are widely used in biological imaging because their unique properties can overcome many drawbacks of conventional organic fluorescent dyes. These QD properties include broad absorption for ease of excitation at multiple wavelengths, narrow emission bands for multicolor imaging, high photostability for longitudinal imaging in cells and *in vivo*, and polyvalency for multifunctional applications.[1−7] Although cadmium- and indium-based QDs exhibit the above desirable properties, concerns remain about the use of these nanomaterials in biological imaging applications.[8,9] To mitigate potential toxicity and provide functionalizable anchors for these QDs, polymer coating has been successfully employed. Not only does this approach significantly increase hydrodynamic diameter (>20 nm), but it also complicates the synthesis procedure and occasionally employs reagents that could induce systemic toxicity. Another unintended consequence of large QDs is that they are generally confined to the vascular space, hindering extravasation from blood vessels and subsequent diffusion to cells distant from the vessels. The combination of large size and prolonged retention in the vascular system favors opsonization and enhanced uptake by the reticuloendothelial system (RES) in the liver. These effects can induce cytotoxicity or reduce QD efficiency and sensitivity in imaging studies.[10]

Recent efforts to overcome size limitations without using toxic materials have resulted in the development of diverse nanoparticle formulations and constructs for *in vivo* applications. Of particular interest

* Address correspondence to achilefus@mir.wustl.edu.

Received for review July 10, 2014 and accepted January 5, 2015.

Published online January 05, 2015
10.1021/nn5071183

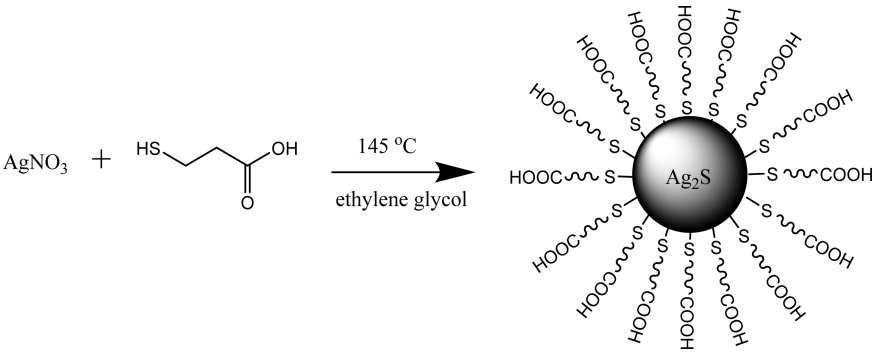

Scheme 1. Synthetic procedure for constructing water-soluble Ag_2S QDs with emission up to 820 nm.

is the potential to develop an array of luminescent silver sulfide (Ag_2S) nanoparticles within a narrow size range. Monoclinic Ag_2S QDs with a bulk band gap of 1.1 eV and a large absorption coefficient have been used in many applications, including photoconductors, photovoltaic cells, and infrared detectors.[11−14] For *in vivo* application, studies have shown that Ag_2S QDs exhibit negligible toxicity in organisms.[15] However, a major challenge is the difficulty in synthesizing multiple Ag_2S QDs with distinct emissions in the near-infrared (NIR) window (750 to 1000 nm), where higher imaging depth can be achieved without complications from tissue autofluorescence. Unfortunately, the widely used synthetic conditions in organic solvents do not adequately control the growth of semiconductor crystals.[16−18] As nanoparticle size approaches that of the bulk crystals, the loss of strong quantum confinement prevents size-dependent tuning of the emission spectra.

In this study, we used two orthogonal approaches to successfully develop water-soluble Ag_2S QDs with a wide range emission (from 520 to 1150 nm). To deliver the QDs selectively into tumor cells and tissue, we conjugated a cyclic peptide, arginine-glycine-aspartic acid-(D)phenylalanine-lysine (cRGDfk) to the QDs for targeting the $\alpha_v\beta_3$ integrin receptor (ABIR),[19−23] which is up-regulated in tumor cells.[24,25]

RESULTS AND DISCUSSION

Synthesis of Ag_2S QDs in Viscous Media to Produce an Array of Distinct Luminescent Nanoparticles. A variety of methods have been developed for the synthesis of visible and extended NIR luminescent QDs.[16,17] In particular, because of quantum confinement effects, the size of Ag_2S QDs could be tuned by modulating the reaction time.[26] Previous studies have shown that a one-pot aqueous synthesis method can produce water-soluble Ag_2S QDs in the visible wavelengths.[15] However, the fast nucleation and growth of Ag_2S in aqueous medium (within a few seconds) leads to rapid transformation to extended NIR emission, making it difficult to obtain good yields of the QDs in the optical "transparent" spectral window between 750 and 900 nm. To overcome this limitation, we employed ethylene glycol as the reaction medium. The higher viscosity of this solvent sufficiently slowed the reaction to enable the isolation of QDs with distinct emission wavelengths from 500 to 820 nm. This was achieved by heating a mixture of $AgNO_3$ and 3-mercaptopropionic acid in ethylene glycol at 145 °C (Scheme 1), followed by quenching the reaction at different time points between 10 and 25 min to afford different fluorescent QDs (see Supporting Information Figure S1 and Methods section).

Next, we explored the application of a viscosity-mediated synthesis procedure to prepare Ag_2S QDs with distinct NIR and extended NIR light-emission in the 840 to 1200 nm spectral range. This reaction is typically performed in organic solvents at high temperatures.[16] Similar to the aqueous reaction conditions, the difficulty in controlling crystal growth under high temperature organic synthesis resulted in Ag_2S QDs with emission close to the band gap (1300 nm) within a short reaction time. To overcome this problem, we used the highly viscous heat transfer organic fluid, Dowtherm A, for this synthesis. Reaction of a mixture of silver diethyldithiocarbamate, oleic acid, and hexadecylamine in Dowtherm A afforded well dispersed hydrophobic Ag_2S QDs. The rapid formation of the monodispersed QDs (within 2 min) was indicated by a change in the color of the reaction mixture, from colorless to brown. The reaction was quenched at different time points between 2 and 30 min and the ensuing hydrophobic QDs were rendered hydrophilic by coating them with tetraethyl orthosilicate (Scheme 2). Thus, the strategic use of solvent viscosity enabled us to obtain an array of distinct visible to extended NIR light-emitting Ag_2S QDs, with the thin silica coating ensuring that the QD diameter remained under 10 nm in all cases (Supporting Information Table S1). X-ray diffraction (XRD) was used to determine the crystal structure of the Ag_2S nanocrystals. Positions of the diffraction angle and the relative intensities of the peaks correlated with the monoclinic crystalline structure of the Ag_2S QDs (Supporting Information Figure S2).

Size-Dependent Optical Properties of Ag_2S QDs. For both synthetic methods used in this study, the absorption and emission spectra of the NIR Ag_2S QDs

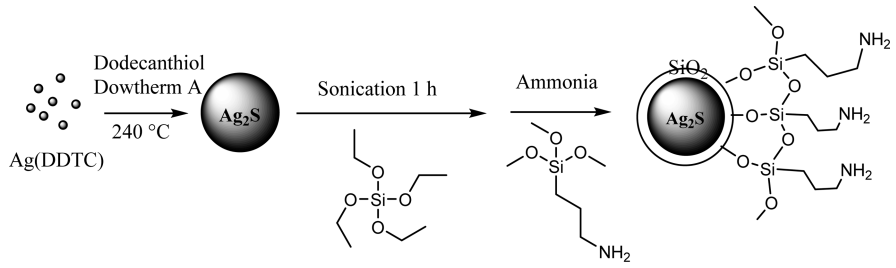

Scheme 2. Synthetic procedure for silica-coated Ag_2S QDs with emission wavelengths in the 840 to 1200 nm spectral range.

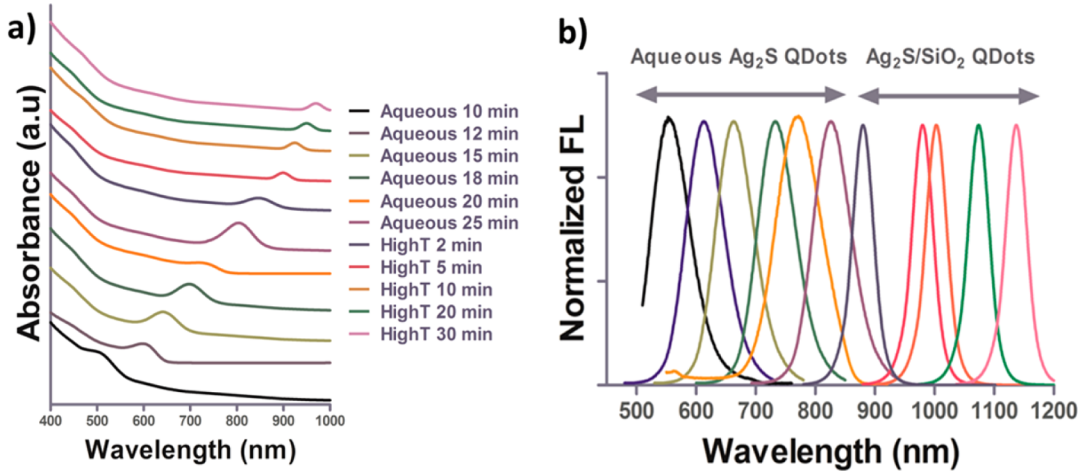

Figure 1. Temporal evolution of the optical properties of Ag_2S QDs. Absorption (a) and normalized emission spectra (b) of Ag_2S QDs and Ag_2S/SiO_2 QDs.

(excitation: 488 nm), prepared in ethylene glycol, and the NIR/extended NIR Ag_2S/SiO_2 (excitation: 785 nm), prepared in Dowtherm A, showed temporal evolution of QD growth (Figure 1 and Supporting Information Table S1). Direct correlation of the emission wavelengths and quantum yields with QD size demonstrates a simple approach to tune their optical properties. In addition, the time-dependent enhancement of the quantum yields suggests that longer reaction times enhanced passivation of the QD surface. The optical properties of the QDs remained stable under continuous illumination with a tungsten lamp (5 mW/cm^2) for up to 24 h, demonstrating the potential use of Ag_2S QDs for longitudinal imaging without loss of fluorescence over time (Supporting Information Figure S3). Similarly, the retention of size distribution and fluorescence intensity at 4 °C for 30 days showed the long shelf life of the nanomaterials (Supporting Information Figure S3).

Conjugation and Determination of the QD to Peptide Ratios. An important goal of this study was to investigate the feasibility of selectively delivering the Ag_2S QDs to cancer cells and tissue. We chose the peptide cRGDfK for this study because it is easy to prepare on solid support and previous studies have shown its high binding affinity to ABIR, which is widely expressed in diverse cancer cells and tumor-associated blood vessels.[27,28] For NIR fluorescence imaging of cells and deep tissues, we used the 820 nm emitting Ag_2S QDs as representative QDs to prepare the QD−peptide conjugates.

First, the cRGDfK was prepared on solid support, as previously reported.[29] A preactivated solution of the QDs was added to the peptide to afford the peptide-labeled cRGDfK-Ag_2S QDs (Scheme 3). The purified conjugate was characterized by both transmission electron microscopy (TEM; Supporting Information Figure S4) and dynamic light scattering (DLS; Supporting Information Figure S5), which exhibited core size and hydrodynamic diameter of less than 10 nm. The TEM images and DLS measurements of the conjugated QDs show that cRGDfK-Ag_2S QDs have an ultrasmall hydrodynamic diameter of about 8 nm, which is much smaller than that of the QD conjugates used in conventional studies.[30−32] Passivation of the Ag_2S QDs by mercaptopropionic acid was confirmed by the characteristic peak of a carboxylate group at 1700 (C═O stretch) and 1350 (C−O stretch) cm^{-1} in the FTIR spectrum (Supporting Information Figure S6). Subsequent conjugation of cRGDfK to the QDs was indicated by the emergence of two new peaks at around 3300 and 3450 cm^{-1} (N−H stretch) from the amine and amide groups, demonstrating successful conjugation and immobilization of cRGDfK peptide on the surface of Ag_2S QDs.

Second, we determined the number of peptides per single QD by reacting Rhodamine 6G (R6G) dye with

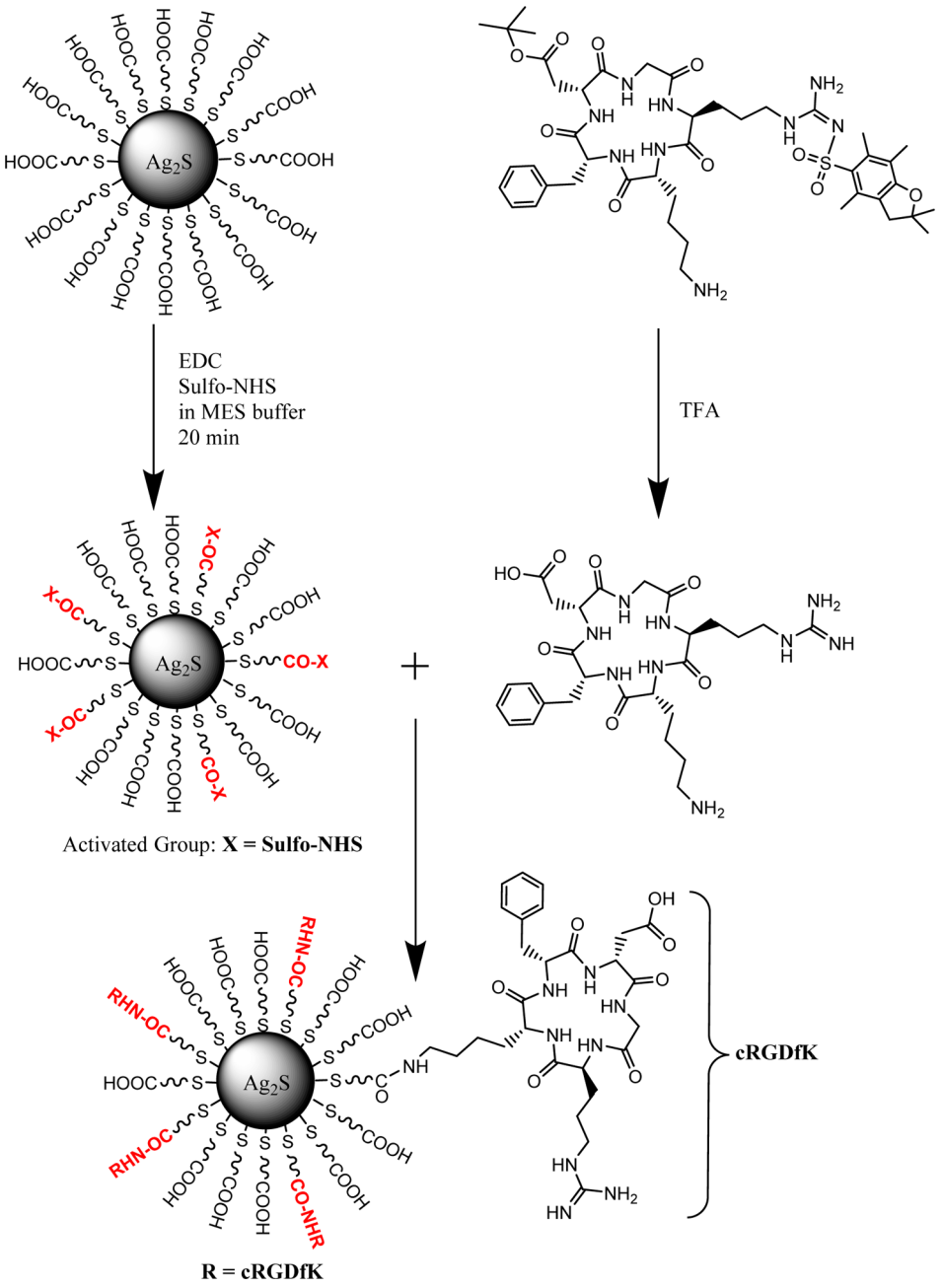

Scheme 3. Schematic of the conjugation procedure for cRGDfK-Ag_2S QDs.

ethylene diamine to yield R6G aminoethylamine, followed by reaction of the resultant free amine with the side-chain aspartic acid moiety of the cRGDfK peptide (Supporting Information Scheme S1). R6G fluorescence (~600 nm) is distinct from that of Ag_2S QDs (820 nm), which provides excellent readout for ratiometric determination of the QD-to-dye fluorescence. This cRGDfK-R6G peptide was then conjugated to the QDs under similar reaction conditions described above to produce cRGDfK-Ag_2S QDs. Analysis of the ratiometric absorption profiles under different conjugation ratios (Supporting Information Figure S7) showed that the QD-to-dye conjugation saturated at a 1:5 ratio. This indicates that the maximum conjugation capacity of the cRGDfK-R6G peptide per single QD is about 5. A similar outcome was determined from the fluorescence ratio of the R6G-cRGDfK-Ag_2S QDs (Supporting Information Figures S8 and S9), confirming the ratio determined by the absorption method. On the basis of the assumption that R6G does not significantly alter the conjugation of the cRGDfK peptide to Ag_2S QDs, we used the 5:1 cRGDfK/QD ratio to calculate the concentrations of solutions used in the biological study. Because the absorption of the QDs was not altered by the peptide conjugation, we used equivalent QD absorptions for nonpeptide-labeled QDs.

Binding Affinity Constant of cRGDfK-Ag_2S QDs to ABIR. Unlike large antibodies, the binding affinity of peptides

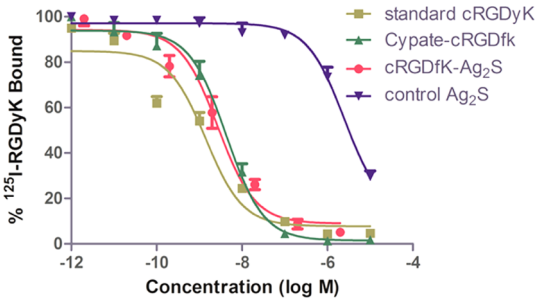

Figure 2. Receptor-binding parameters of ABIR-binding peptides and control Ag_2S QDs.

can be easily altered upon conjugation to relatively larger reporter systems, such as QDs. Using the ratio of 5 peptides per QD, purified human ABIR protein, and radiolabeled ^{125}I-RGDyK as a tracer, we investigated the ABIR binding affinity of the cRGDfk peptides on the QD surface to ABIR (see Methods section).[22] Nonspecific binding of ^{125}I-c(RGDyK) was determined to be 5−10% of the total binding. The 50% inhibitory concentrations (IC_{50}) and affinity constants (K_i) were calculated by nonlinear regression analysis[22] (Figure 2 and Table 1). The results demonstrate that cRGDfK retained its ABIR binding affinity after conjugation to Ag_2S QDs, as evidenced by similarity of the K_i for the conjugated peptide to that of the standard ABIR-avid peptide (cRGDfK) and a small NIR fluorescent dye-labeled peptide (Cypate-cRGDfK).[22] The one log unit improvement in the K_i of cRGDfK-Ag_2S QDs relative to Cypate-cRGDfK could be attributed to enhanced avidity caused by multivalent interactions of the peptides per particle with ABIRs.

ABIR-Mediated Cellular Internalization and Cytotoxicity of cRGDfK-Ag_2S QDs. We investigated the selective uptake of peptide labeled QDs relative to the nonconjugated Ag_2S QDs in mouse breast cancer (4T1luc) cell lines, which overexpress ABIR. Using a fluorescence microscope, images of the nuclei (excitation (Ex)/emission (Em): 488 nm/515−560 nm) and QD distribution (Ex/Em: 710 ± 35 nm/810 ± 45 nm) were acquired, and fluorescence intensity (FI) was processed using NIH ImageJ software. Unlike many hard shell nanoparticles, which internalize in cells nonspecifically by various mechanisms, the time course imaging showed negligible internalization of Ag_2S QDs in cells up to 24 h of incubation (Figure 3). This behavior is similar to that of small negatively charged hydrophilic dyes, which do not internalize in cells due to charge−charge repulsion caused by the negatively charged phosphate-rich cell membranes. In contrast, the cRGDfK-Ag_2S QDs exhibited significant intracellular NIR fluorescence within 1 h of incubation, which continued to increase up to 24 h (Figure 3). We then extended the study to human cancer cell models. Incubation of A549 human lung adenocarcinoma epithelial cells, which also overexpress ABIR, with Ag_2S QDs or cRGDfK-Ag_2S QDs showed an internalization pattern similar to the 4T1luc cells (Supporting Information Figure S10).

TABLE 1. ABIR Binding Parameters (IC_{50} and K_i) for Different Integrin-Avid Peptides

compd[a]	IC_{50} (nM) (mean ± SD)	K_i (nM) (mean ± SD)	R^2
cRGDyK	1.42 ± 0.38	0.92 ± 0.25	0.9434
Cypate-cRGDfK	4.29 ± 0.56	2.77 ± 0.36	0.9900
cRGDfK-Ag_2S QDs	2.74 ± 0.94	1.77 ± 0.61	0.9740

[a] The binding affinity for the control Ag_2S QDs was too low for determination under our measurement conditions.

To confirm ABIR-mediated internalization of cRGDfK QDs in cells, we preincubated the cells with cRGDfK peptide for 1 h, followed by incubation with cRGDfK-Ag_2S QDs for another 18 h. Fluorescence imaging showed that the uptake of cRGDfK-Ag_2S QDs by tumor cells was successfully blocked by the free peptide in two different ABIR expressing cell lines (Figure 4).[33]

Using the thriazolyl blue tetrazolium bromide (MTT) cytotoxicity assay, we evaluated the toxicity of Ag_2S QDs, cRGDfk-Ag_2S conjugates, and Ag_2S @SiO_2−NH_2 QDs in one nontumor and three tumor cell lines: PMEC (primary mammary epithelial cells, normal cells), 4T1luc, A549, and the human epithelial carcinoma cell line A431. The results show that cell viability was about 100% for all cell lines after treatment with 10 μM of each nanomaterial at a concentration that is much higher than required for biological imaging (Figure 5 and Supporting Information Figure S11). Although some studies have indicated that Ag_2S nanoparticles have the potential for serious toxicity,[34] it is possible that toxicity depends on the type of nanoparticles used, including confounding factors such as coating materials and impurities. However, long-term toxicity studies, including the activation of oncogenes, are needed to conclusively determine the safety profiles of these materials.

Longitudinal Noninvasive Imaging and Histologic Validation of cRGDfK-Ag_2S QDs Distribution in 4T1luc Tumor Bearing Rodents. The ease of preparing extended NIR photoluminescence Ag_2S QDs has ushered in new interest in the application of Ag_2S QDs for cancer imaging in the 1200 nm emission range.[16,17] A current challenge is that most *in vivo* NIR fluorescence imaging systems available today are optimized for light detection in the classical 700−900 nm range, making it difficult to study the whole-body dynamic distribution of NIR nanomaterials in rodents and in real-time.

We addressed the above challenges in our study by (1) developing stable Ag_2S QDs with optimal excitation/emission at 785/820 nm, using viscous solvents to control QD growth, (2) coating the surface of the QDs with small reactive molecules to retain small hydrodynamic size, and (3) conjugating small peptides to the QDs for tumor-targeted delivery without relying on EPR effect.

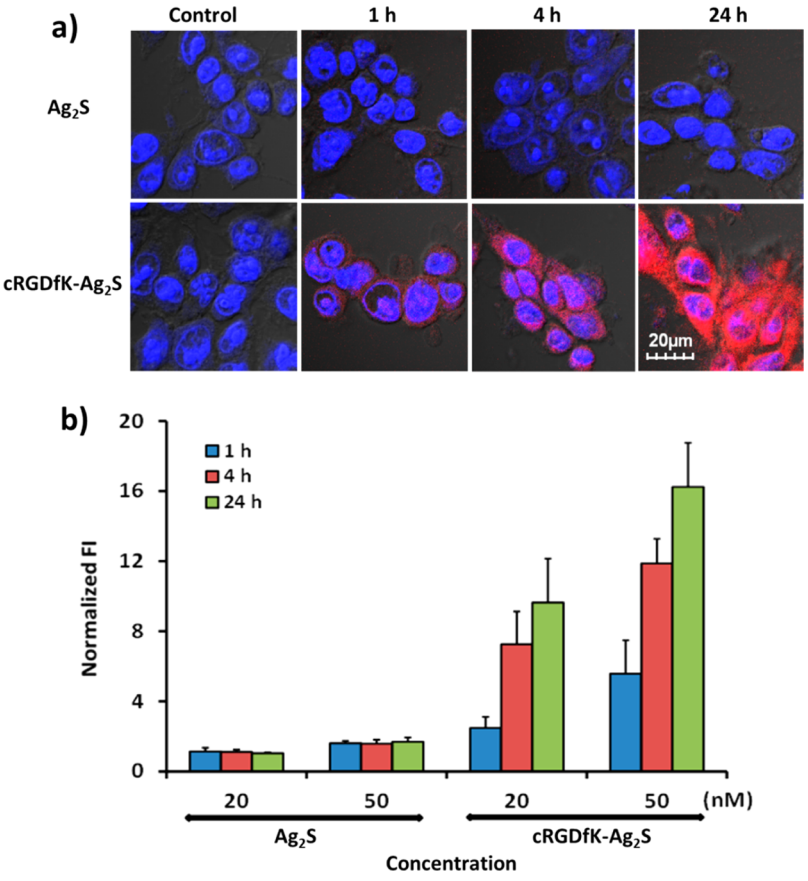

Figure 3. Evaluation of internalization of QDs in 4T1luc cells at different time points: (a) 20 nM of cRGDfK-Ag_2S QDs (red) began to internalize within 1 h and increased up to 24 h of incubation. Fluorescence of cells treated with the control Ag_2S QD remained low for the duration of the study period. (b) Quantitative analysis of the fluorescence intensity (FI) of images in panel a; all FI are normalized to background fluorescence.

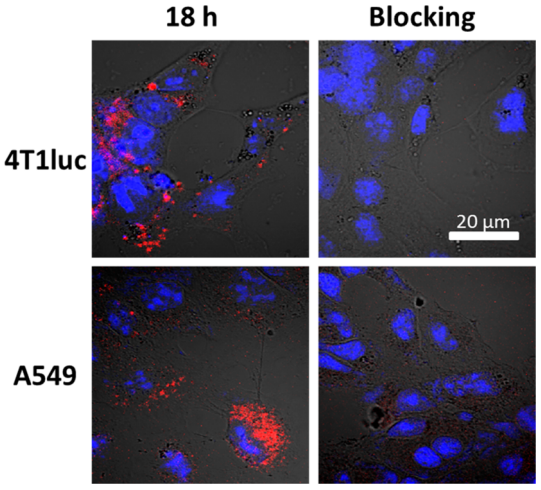

Figure 4. Internalization (left) and inhibition (right) of cRGDfK-Ag_2S QDs in 4T1luc and A549 cells using 2 μM cRGDfK peptide and 20 nM cRGDfK-Ag_2S QDs. Red, QD fluorescence; blue, nuclear stain.

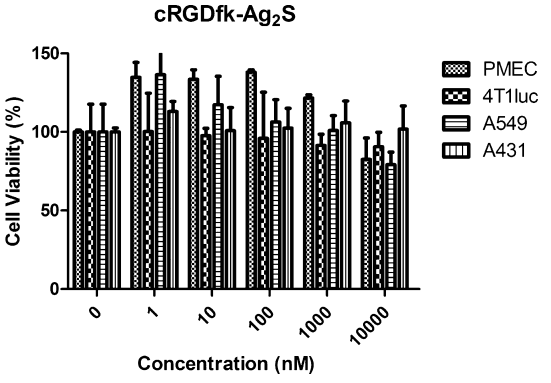

Figure 5. MTT-based cell viability assays of PMEC, 4T1luc, A549, and A431 cells treated with various concentrations of cRGDfK-Ag_2S QDs.

To investigate the biodistribution profile of the QDs in rodents, we developed subcutaneous 4T1luc tumors on the bilateral flanks of Balb/c mice (Figure 6). The mice were injected intravenously with cRGDfK-Ag_2S QDs, and a control population was injected with nonpeptide labeled Ag_2S QDs. Noninvasive fluorescence images were acquired at 1, 4, and 24 h postinjection. Similar to the cell studies, Ag_2S QDs were not selectively retained in tumors after the initial nonspecific distribution throughout the body (Supporting Information Figure S12). High fluorescence in the bladder and residual fluorescence in tumor, intestines, and kidneys at 4 h postinjection suggests rapid clearance by the hepatobiliary and renal pathways. By 24 h, fluorescence was not detectable throughout the body,

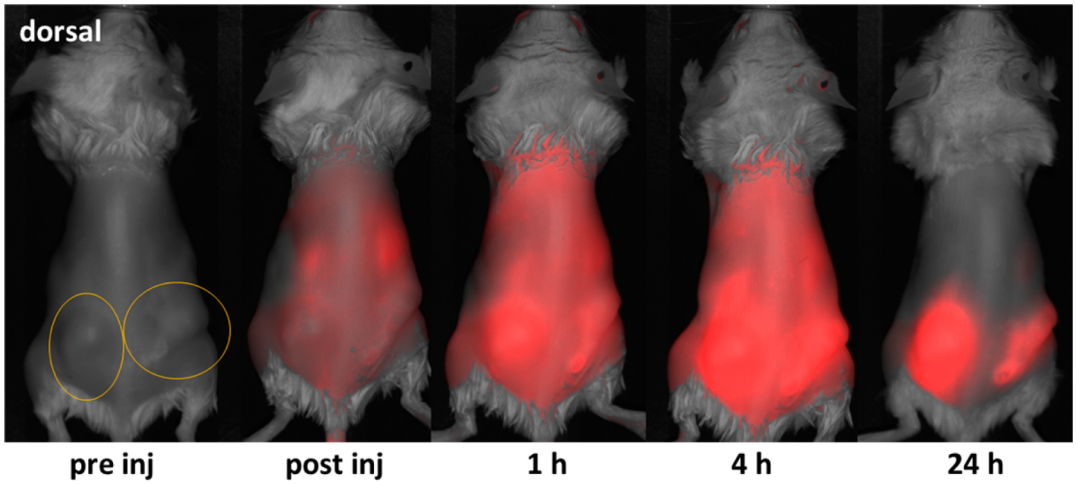

Figure 6. Representative *in vivo* fluorescence imaging of cRGDfK-Ag_2S in 4T1luc tumor-bearing Balb/c mouse at different time points after intravenous administration. Circles indicate bilateral subcutaneous tumor locations. Red color: QD fluorescence.

minimizing the potential for long-term systemic and organ toxicity.

In contrast, mice treated with cRGDfK-Ag_2S QDs were widely distributed all over the tissue immediately after injection, but concentrated around the tumors within 1 h (Figure 6). Longitudinal imaging showed excellent tumor uptake with minimal background fluorescence at 24 h postinjection. Previous studies with extended NIR fluorescent QDs showed high uptake of the Ag_2S QDs in the liver and spleen, which is characteristic of many nanoparticles used for *in vivo* imaging studies. In this case, the small hydrodynamic size of cRGDfK-Ag_2S QDs resulted in biodistribution profiles similar to small organic molecules, but with the added advantage of photostability and multivalency. This provides a clear path for using these QDs as models for drug delivery and imaging treatment response.

We also investigated the temporal *in vivo* distribution of cRGDfK-Ag_2S QDs in the A431 mouse model. Bilateral tumors were developed in the flanks of nude mice and noninvasive imaging was conducted as described above. Tumor uptake was evident within 1 h postinjection, with high tumor-to-background fluorescence achieved by the 5 h time point (Supporting Information Figure S13). *Ex vivo* fluorescence imaging and fluorescence intensity analysis at 24 h postadministration exhibited an excellent biodistribution profile, similar to data obtained with the 4T1luc tumor model. These results demonstrate the potential applicability of the QDs for imaging tumors that express high levels of ABIR.

To validate the high tumor-selective uptake of cRGDfK-Ag_2S QDs seen in noninvasive fluorescence imaging, major organs and tissues were imaged *ex vivo* after the 24 h time point (Figure 7a). Whereas the shallow penetration of light in deep tissues obscured detection of QD emission from the liver and kidneys (Figure 6), *ex vivo* imaging showed significant fluorescence from these organs (Figure 7 a,b), illustrating the importance of *ex vivo* validation of the noninvasive fluorescence distribution. Apart from the expected excretion organs (liver and kidneys), which exhibited some NIR fluorescence, the net sum of fluorescence in the two tumor tissues indicates that the majority of the cRGDfK-Ag_2S QDs accumulated in tumor tissues (Figure 7b). Noteworthy is the low uptake in the spleen, indicating that the QDs do not exhibit particulate properties *in vivo*. Relative to the surrounding tissue, an excellent tumor-to-muscle ratio of about 9:1 was obtained.

Analysis of spatial distribution of the cRGDfK-Ag_2S QDs in tumors is important to determine if the QDs are clustered in one area (indication of EPR) or dispersed throughout the tumor tissue (indicative of extravasation and diffusion). Using a cross section of the tumor, we imaged the NIR fluorescence (see Methods section). The results show that cRGDfK-Ag_2S QD fluorescence was detected in different sections of the tumor, including the periphery and interior regions (Figure 7c). Infiltration of the tumor cells into adjoining muscle tissue appears to be tracked by the QDs (Figure 7c, lower right). This finding supports a model in which the small cRGDfK-Ag_2S QDs extravasate into tumor tissue, bind to ABIRs, and subsequently internalize in tumor cells via receptor-mediated endocytosis.

We confirmed the internalization of cRGDfK-Ag_2S QDs in tumor cells from the excised tumor tissue using TEM (Figure 8). A few areas of dark deposits were found in different regions of the tumor tissue. These deposits contained smaller diffuse particles in the size range of the QDs. The QDs were clustered in a subcellular location that appeared to be endocytic vesicles. This suggests that cRGDfK-Ag_2S QD internalization was mediated by endocytosis.

CONCLUSION

We have developed a modular and simple approach to prepare stable water-soluble NIR Ag_2S QDs covering a wide spectral window from 500 to 1200 nm.

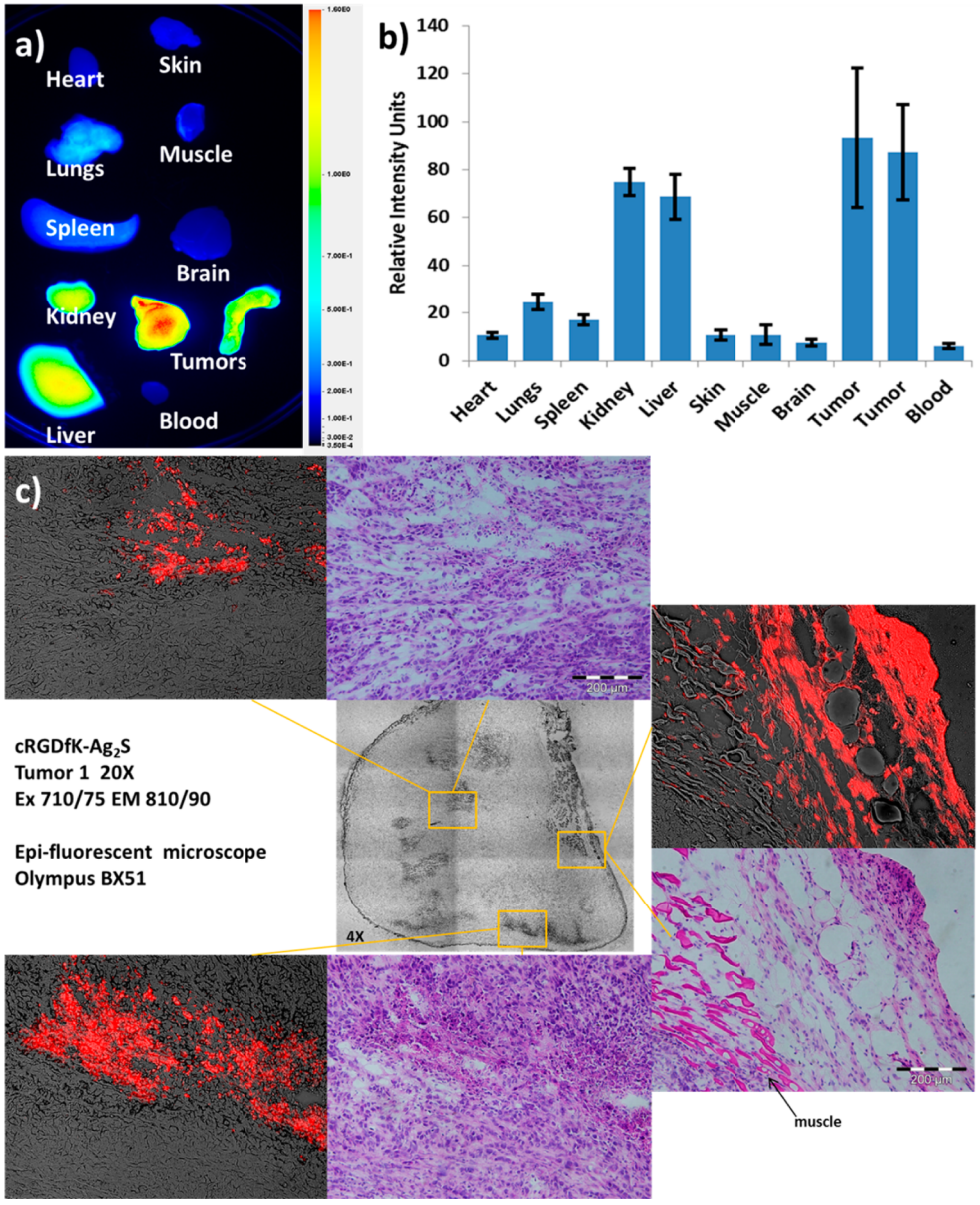

Figure 7. (a) Representative *ex vivo* fluorescence image of organ tissues from 4T1luc bilateral tumor bearing mice 24 h postinjection. (b) Relative fluorescence intensity analysis of different organs and tissues; three Balb/c mice, three nude mice, and two A431 tumors were used in this study. (c) NIR fluorescence (20×) and hematoxylin and eosin (H&E) stained images of QDs in tumor tissue. Brightfield image is 4× cross section of the entire tumor. Boxes indicate areas of the tumor that show NIR fluorescence. The tissue was subsequently stained with H&E , and the same areas were imaged to correlate with the fluorescence data. Fluorescent cells are seen on the tumor periphery and interior, with possible interior necrotic areas. Tumor cells infiltrating into adjoining muscle tissue were visible in both the NIR fluorescence and H&E staining. Scale bar: 200 μm.

Using representative Ag_2S QDs, we successfully conjugated a tumor-avid peptide, cRGDfK, to the QDs. The combination of a small QD core, coating, and tumor-targeting peptide maintained the hydrodynamic diameter at less than 10 nm. Both cell and small animal studies demonstrate the high selective uptake in tumor cells and tissue, respectively. Unlike most hardcore nanoparticles, higher uptake of cRGDfK-Ag_2S QDs was observed in tumors relative to either the kidneys or liver. The simplicity of synthesis, significant renal excretion of unbound QDs, rapid extravasation to tumor tissue, and selective retention in tumors supports the use of this nanoplatform for molecular imaging of diseases and the monitoring of treatment response.

METHODS

Materials. Silver nitrate, 3-mercaptopropionic acid, ethylene glycol, silver diethyldithiocarbamate [Ag(DDTC)], 1-dodecanethiol, (3-aminopropyl)trimethoxysilane (APTMS), tetraethyl orthosilicate (TEOS), and Dowtherm A were purchased from Sigma-Aldrich (St. Louis, MO), 1-ethyl-3-[3-(dimethylamino)propyl]-carbodiimide hydrochloride(EDC) and *N*-hydroxysulfosuccinimide-(sulfo-NHS) were purchased from Thermo Fisher Scientific

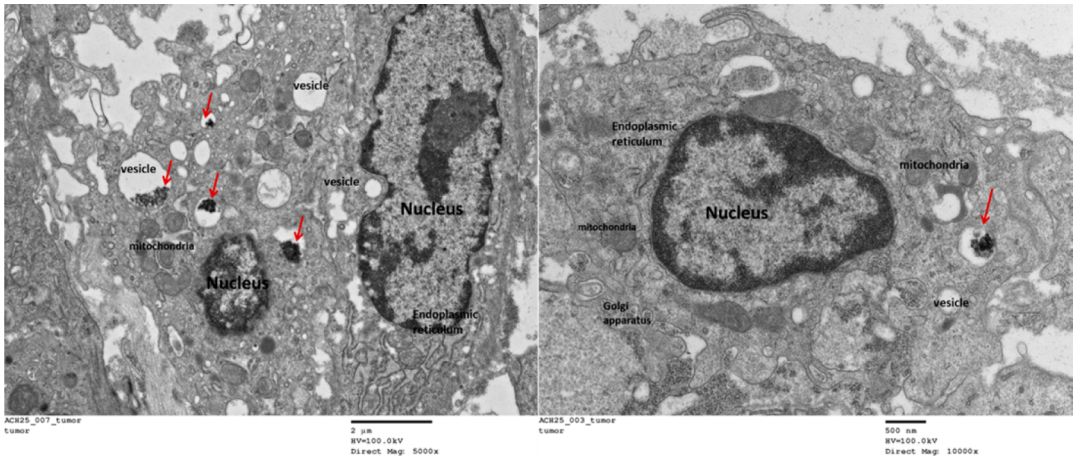

Figure 8. TEM analysis of cRGDfK-Ag_2S QDs internalized into tumor cells. Red arrows indicate cRGDfK-Ag_2S QD accumulation. Scale bar: 2 μm (left) and 0.5 μm (right).

(Rockford, IL), and all of the amino acids were purchased from Novabiochem (Philadelphia, PA).

Synthesis of Aqueous Ag_2S QDs up to 820 nm. Silver nitrate (51 mg, 0.3 mmol) and 3-mercaptopropionic acid (0.5 μL, 7 mmol) were mixed with 4.5 mL of ethylene glycol. The reaction mixture was degassed for 10 min before refilling with dry argon. The mixture was then heated to 145 °C for the QD growth (Scheme 1). The reaction turned from cloudy white to slightly yellow and eventually became clear after 10 min (Supporting Information Figure S1), at which time fluorescence of the QDs was first observed. The reaction mixture gradually turned darker, and the growth was quenched by rapidly cooling the reaction mixture in ice water at different time points (10, 12, 15, 18, 20, and 25 min). Purification of the QD products was performed by three rounds of centrifugation and redispersal of the collected pellets in water.

Synthesis of Water-Soluble Silica Coated Ag_2S QDs from 880 to 1150 nm. Silver diethyldithiocarbamate (77 mg, 0.3 mmol), oleic acid (1 mL), and hexadecylamine (240 mg) were mixed with 9 mL of Dowtherm A in a 50 mL reaction tube. The reaction mixture was then degassed and refilled with dry argon several times with vigorous stirring. The reaction mixture was heated to 200 °C for QD growth under argon. The reaction was quenched at different time points (2, 5, 10, 20, and 30 min, respectively) to obtain different sizes of the product. Subsequently, methanol was poured into the reaction aliquot, and the QD products were collected by centrifugation.

TEOS (1 mL) was added to the pellet, and the sample was sonicated for 1 h. Extra APTMS and ammonia solution (10%) were added to the mixture, and it was sonicated for an additional hour. The product was centrifuged and the supernatant decanted. The collected pellets were redispersed in water or PBS for optical measurement, morphology characterization, and subsequent use.

Peptide Synthesis and Conjugation with Ag_2S QDs. Cyclic-RGDfK was prepared as previously reported.[29] Conjugation of the peptide with QDs was performed via EDC using sulfo-NHS chemistry.[35] Briefly, Ag_2S QDs in MES buffer (50 nM, 1 mL) were added to EDC (0.4 mg) and sulfo-NHS (1.1 mg). The reaction mixture was vortexed at room-temperature for 20 min, the QDs were precipitated by centrifugation, and the supernatant was discarded. The QDs were redispersed in PBS and the cRGDfK peptide (0.61 mg, 1 μmol) in a small amount of DMSO was added to the QDs (Scheme 3). The vortexing continued for another 2 h at RT. The cRGDfK-Ag_2S QDs were purified by centrifugation and redispersed in water or PBS several times for spectroscopy, morphology, and biological studies.

Spectral Properties Measurement. The optical spectra were recorded using a spectrophotometer (Beckman Coulter DU640), Fluorolog-3 Spectrofluorometer (Jobin Horiba, Yvon), and VIS-NIR spectrofluorometer (Custom built, Jobin Horiba Yvon).

Solid-Phase Receptor-Binding Determination. A competitive radiolabeled receptor binding assay was used to determine the binding affinity of the cRGDfk peptide on the QD surface to ABIR. The receptor binding assays were carried out using human integrin $\alpha_v\beta_3$ purified protein (Chemicon International, Inc., Temecula, CA) in a 96 well White Polystyrene Medium Binding Stripwell Microplate (Corning Headquarters, Corning, NY). The microplates were coated with ABIR purified protein (500 ng/mL; 100 μL per well) in coating buffer (25 mM Tris-HCl, pH 7.4, 150 mM NaCl, 1 mM $CaCl_2$, 1 mM $MgCl_2$, and 1 mM $MnCl_2$) for 16 h at 4 °C. The wells were then blocked for 2 h with 150 μL of binding buffer (coating buffer with 0.5% bovine serum albumin). After two washes with binding buffer, the plates were incubated with ^{125}I-RGDyK (2 nmol/L) in the presence of various concentrations of ligand ranging from 1 pM to 10 μM for 16 h at room temperature, followed by three washes with binding buffer. The radioactivity of c(RGDyK) peptide bound to ABIR was counted using a Packard Cobra II Autogamma counter (Meriden, CT). Nonspecific binding of ^{125}I-c(RGDyK) was determined to be 5 to 10% of the total binding. The 50% inhibitory concentrations (IC_{50}) and affinity constants (K_i) were calculated by nonlinear regression analysis using GraphPad Prism 4 software (GraphPad Software, Inc., San Diego, CA). All samples were analyzed in triplicate.

Cell Culture and Inhibition of cRGDfK-Ag_2S QDs Uptake by Cells. All cell lines were incubated in 95% air/5% CO_2 at 37 °C. The mouse breast cancer 4T1luc cell line (Sibtech, Brookfield, CT) was cultured in RPMI-1640 medium supplemented with 10% FBS, 1.5 mg/mL $NaHCO_3$, and 2 mM L-glutamine. The human lung cancer A549 cell line (ATCC, Manassas, VA) was cultured in Ham's F-12K medium. For imaging studies, 1×10^4 cells/well were grown on LabTek 8-chamber slides (Nunc Inc. Rochester, NY) overnight. 4T1luc cells were incubated with control Ag_2S and cRGDfK-Ag_2S QDs at different concentrations in culture medium at 37 °C. The samples were analyzed at different time points. For blocking studies, 4T1luc and A549 cells were preincubated with 2 μM of cRGDfK in culture medium for 1 h and then incubated with a mixture of unlabeled cRGDfK (2 μM) and cRGDfK-Ag_2S QDs (20 nM) for another 18 h at 37 °C. After 3 washes with PBS (pH 7.4), cells were fixed with 4% paraformaldehyde for 5 min and treated with 1:2000 ToTo1 (Invitrogen) for 1 h at 37 °C. Slides were mounted, coversliped, and sealed with nail polish. A DP71 Olympus microscope was used to image all samples, using Ex/Em = 488 nm/515−560 nm for nuclei and Ex/Em = 710 ± 35 nm/810 ± 45 nm for QDs. Fluorescence intensity in the cells was processed using NIH ImageJ software and then normalized to FI of the background.

Cell Viability. The cytotoxicity of cRGDfK-Ag_2S QDs was examined using a conventional MTT assay employing two different cancer cell lines, 4T1luc and A549. Cells were seeded in 96-well plates at a density of 1×10^4 cells per well and incubated for 24 h at 37 °C. After removing the culture medium, the wells were washed with PBS. The media in each well was then replaced with 90 μL of fresh media and 10 μL of QDs in PBS. After another 24 h incubation, thriazolyl blue tetrazolium bromide (MTT, Sigma-Aldrich, St. Louis, MO) was added to each

well for a final concentration of 0.5 mg/mL and incubated for another 4 h. DMSO (100 μL) was added to solubilize the MTT−formazan product, and the absorbance of the solution was read at 540 nm.

In Vivo and ex Vivo Tumor Imaging of Breast Cancer. Animal studies were performed in accordance with protocols approved by the Washington University School of Medicine Animal Studies Committee. Three Balb/c were injected subcutaneously on bilateral flanks and three nude mice were injected orthotopically with 4T1luc tumor cells (5×10^5 cells). When the tumors had grown to about 5 mm in diameter, the mice were injected by tail vein with cRGDfK-Ag_2S QDs or Ag_2S QDs, which served as nonpeptide control. Mice were imaged with the Pearl imager (LiCor, Lincoln, NE) at different points (preinjection, immediately postinjection, 1, 4, and 24 h). The mice were then sacrificed, and *ex vivo* biodistribution was determined. Tumors were harvested and frozen in OCT (Fisher Scientific, Hampton, NH) for tissue analysis. A similar procedure was used for the subcutaneous model of A431 tumors.

Transmission Electron Microscopy. For ultrastructural analysis, 1 mm^3 pieces of tumor tissue were fixed in 2% paraformaldehyde/2.5% glutaraldehyde (Polysciences Inc., Warrington, PA) in 100 mM sodium cacodylate buffer, pH 7.2 for 2 h at room temperature. Samples were washed in cacodylate buffer and postfixed in 1% osmium tetroxide (Polysciences Inc.) for 1 h, followed by extensive rinses in dH_2O before staining with 1% aqueous uranyl acetate (Ted Pella Inc., Redding, CA) for 1 h. Following several rinses in dH_2O, samples were dehydrated in a graded series of ethanol and embedded in Eponate 12 resin (Ted Pella Inc.). Sections of 95 nm were cut with a Leica Ultracut UCT ultramicrotome (Leica Microsystems Inc., Bannockburn, IL), stained with uranyl acetate and lead citrate, and viewed on a JEOL 1200 EX transmission electron microscope (JEOL USA Inc., Peabody, MA) equipped with an AMT 8 megapixel digital camera (Advanced Microscopy Techniques, Woburn, MA).

Conflict of Interest: The authors declare no competing financial interest.

Acknowledgment. This study was supported in part by grants from the National Institutes of Health (NCI, R01 CA171651 and P50 CA094056; NIBIB, R01 EB00811; and NHLBI, HHSN268201000046C).

Supporting Information Available: Additional visual and spectroscopic information, cell study, and TEM images. This material is available free of charge *via* the Internet at http://pubs.acs.org.

REFERENCES AND NOTES

1. Lim, Y. T.; Kim, S.; Nakayama, A.; Stott, N. E.; Bawendi, M. G.; Frangioni, J. V. Selection of Quantum Dot Wavelengths for Biomedical Assays and Imaging. *Mol. Imaging* **2003**, *2*, 50–64.
2. Smith, A. M.; Gao, X.; Nie, S. Quantum Dot Nanocrystals for In Vivo Molecular and Cellular Imaging. *Photochem. Photobiol.* **2004**, *80*, 377–385.
3. Medintz, I. L.; Uyeda, H. T.; Goldman, E. R.; Mattoussi, H. Quantum Dot Bioconjugates for Imaging, Labelling and Sensing. *Nat. Mater.* **2005**, *4*, 435–446.
4. Pinaud, F.; Michalet, X.; Bentolila, L. A.; Tsay, J. M.; Doose, S.; Li, J. J.; Iyer, G.; Weiss, S. Advances in Fluorescence Imaging with Quantum Dot Bio-Probes. *Biomaterials* **2006**, *27*, 1679–1687.
5. Walther, C.; Meyer, K.; Rennert, R.; Neundorf, I. Quantum Dot-Carrier Peptide Conjugates Suitable for Imaging and Delivery Applications. *Bioconjugate Chem.* **2008**, *19*, 2346–2356.
6. Cao, Y.; Yang, K.; Li, Z.; Zhao, C.; Shi, C.; Yang, J. Near-Infrared Quantum-Dot-Based Non-Invasive In Vivo Imaging of Squamous Cell Carcinoma U14. *Nanotechnology* **2010**, *21*, 475104.
7. Zrazhevskiy, P.; Gao, X. Quantum Dot Imaging Platform for Single-Cell Molecular Profiling. *Nat. Commun.* **2013**, *4*, 1619.
8. Mahendra, S.; Zhu, H.; Colvin, V. L.; Alvarez, P. J. Quantum Dot Weathering Results in Microbial Toxicity. *Environ. Sci. Technol.* **2008**, *42*, 9424–9430.
9. Lin, C. H.; Chang, L. W.; Chang, H.; Yang, M. H.; Yang, C. S.; Lai, W. H.; Chang, W. H.; Lin, P. The Chemical Fate of the vCd/Se/Te-Based Quantum Dot 705 in the Biological System: Toxicity Implications. *Nanotechnology* **2009**, *20*, 215101.
10. Schipper, M. L.; Iyer, G.; Koh, A. L.; Cheng, Z.; Ebenstein, Y.; Aharoni, A.; Keren, S.; Bentolila, L. A.; Li, J.; Rao, J.; *et al.* Particle Size, Surface Coating, and Pegylation Influence the Biodistribution of Quantum Dots in Living Mice. *Small* **2009**, *5*, 126–134.
11. Zhuang, Z.; Peng, Q.; Wang, X.; Li, Y. Tetrahedral Colloidal Crystals of Ag_2S Nanocrystals. *Angew. Chem., Int. Ed.* **2007**, *46*, 8174–8177.
12. Chen, C.; Xie, Y.; Ali, G.; Yoo, S. H.; Cho, S. O. Improved Conversion Efficiency of Ag_2S Quantum Dot-Sensitized Solar Cells Based on TiO_2 Nanotubes with a ZnO Recombination Barrier Layer. *Nanoscale Res. Lett.* **2011**, *6*, 462.
13. Nagasuna, K.; Akita, T.; Fujishima, M.; Tada, H. Photodeposition of Ag_2S Quantum Dots and Application to Photoelectrochemical Cells for Hydrogen Production under Simulated Sunlight. *Langmuir* **2011**, *27*, 7294–7300.
14. Xiao, J. P.; Xie, Y.; Tang, R.; Luo, W. Template-Based Synthesis of Nanoscale Ag_2S (E = S, Se) Dendrites. *J. Mater. Chem.* **2002**, *12*, 1148–1151.
15. Jiang, P.; Zhu, C. N.; Zhang, Z. L.; Tian, Z. Q.; Pang, D. W. Water-Soluble Ag_2S Quantum Dots for Near-Infrared Fluorescence Imaging In Vivo. *Biomaterials* **2012**, *33*, 5130–5135.
16. Du, Y.; Xu, B.; Fu, T.; Cai, M.; Li, F.; Zhang, Y.; Wang, Q. Near-Infrared Photoluminescent Ag_2S Quantum Dots from a Single Source Precursor. *J. Am. Chem. Soc.* **2010**, *132*, 1470–1471.
17. Hong, G.; Robinson, J. T.; Zhang, Y.; Diao, S.; Antaris, A. L.; Wang, Q.; Dai, H. In Vivo Fluorescence Imaging with Ag_2S Quantum Dots in the Second Near-Infrared Region. *Angew. Chem., Int. Ed.* **2012**, *51*, 9818–9821.
18. Zhang, Y.; Hong, G.; Chen, G.; Li, F.; Dai, H.; Wang, Q. Ag_2S Quantum Dot: A Bright and Biocompatible Fluorescent Nanoprobe in the Second Near-Infrared Window. *ACS Nano* **2012**, *6*, 3695–3702.
19. Cardarelli, P. M.; Cobb, R. R.; Nowlin, D. M.; Scholz, W.; Gorcsan, F.; Moscinski, M.; Yasuhara, M.; Chiang, S. L.; Lobl, T. J. Cyclic RGD Peptide Inhibits Alpha 4 Beta 1 Interaction with Connecting Segment 1 and Vascular Cell Adhesion Molecule. *J. Biol. Chem.* **1994**, *269*, 18668–18673.
20. Belvisi, L.; Bernardi, A.; Colombo, M.; Manzoni, L.; Potenza, D.; Scolastico, C.; Giannini, G.; Marcellini, M.; Riccioni, T.; Castorina, M.; *et al.* Targeting Integrins: Insights into Structure and Activity of Cyclic RGD Pentapeptide Mimics Containing Azabicycloalkane Amino Acids. *Bioorg. Med. Chem.* **2006**, *14*, 169–180.
21. Chen, Z.; Deng, J.; Zhao, Y.; Tao, T. Cyclic RGD Peptide-Modified Liposomal Drug Delivery System: Enhanced Cellular Uptake In Vitro and Improved Pharmacokinetics in Rats. *Int. J. Nanomed.* **2012**, *7*, 3803–3811.
22. Edwards, W. B.; Akers, W. J.; Ye, Y.; Cheney, P. P.; Bloch, S.; Xu, B.; Laforest, R.; Achilefu, S. Multimodal Imaging of Integrin Receptor-Positive Tumors by Bioluminescence, Fluorescence, Gamma Scintigraphy, and Single-Photon Emission Computed Tomography Using a Cyclic RGD Peptide Labeled with a Near-Infrared Fluorescent Dye and a Radionuclide. *Mol. Imaging* **2009**, *8*, 101–110.
23. Ye, Y.; Xu, B.; Nikiforovich, G. V.; Bloch, S.; Achilefu, S. Exploring New Near-Infrared Fluorescent Disulfide-Based Cyclic RGD Peptide Analogs for Potential Integrin-Targeted Optical Imaging. *Bioorg. Med. Chem. Lett.* **2011**, *21*, 2116–2120.
24. Kumagai, H.; Tajima, M.; Ueno, Y.; Giga-Hama, Y.; Ohba, M. Effect of Cyclic Peptide on Cell Adhesion and Tumor Metastasis. *Biochem. Biophys. Res. Commun.* **1991**, *177*, 74–82.
25. Lee, H.; Akers, W.; Bhushan, K.; Bloch, S.; Sudlow, G.; Tang, R.; Achilefu, S. Near-Infrared Ph-Activatable Fluorescent

Probes for Imaging Primary and Metastatic Breast Tumors. *Bioconjugate Chem.* **2011**, *22*, 777–784.
26. Kang, K. C.; Min, B. I. Effect of Quantum Confinement on Electron Tunneling through a Quantum Dot. *Phys. Rev. B* **1997**, *55*, 15412–15415.
27. Carmeliet, P.; Jain, R. K. Angiogenesis in Cancer and Other Diseases. *Nature* **2000**, *407*, 249–257.
28. Desgrosellier, J. S.; Cheresh, D. A. Integrins in Cancer: Biological Implications and Therapeutic Opportunities. *Nat. Rev. Cancer* **2010**, *10*, 9–22.
29. Colombo, R.; Mingozzi, M.; Belvisi, L.; Arosio, D.; Piarulli, U.; Carenini, N.; Perego, P.; Zaffaroni, N.; De Cesare, M.; Castiglioni, V.; *et al.* Synthesis and Biological Evaluation (In Vitro and In Vivo) of Cyclic Arginine-Glycine-Aspartate (RGD) Peptidomimetic-Paclitaxel Conjugates Targeting Integrin Alphavbeta3. *J. Med. Chem.* **2012**, *55*, 10460–10474.
30. Bentolila, L. A.; Ebenstein, Y.; Weiss, S. Quantum Dots for In Vivo Small-Animal Imaging. *J. Nucl. Med.* **2009**, *50*, 493–496.
31. Kuo, C. W.; Chueh, D. Y.; Singh, N.; Chien, F. C.; Chen, P. Targeted Nuclear Delivery Using Peptide-Coated Quantum Dots. *Bioconjugate Chem.* **2011**, *22*, 1073–1080.
32. Hu, R.; Law, W. C.; Lin, G.; Ye, L.; Liu, J.; Reynolds, J. L.; Yong, K. T. Pegylated Phospholipid Micelle-Encapsulated Near-Infrared Pbs Quantum Dots for In Vitro and In Vivo Bioimaging. *Theranostics* **2012**, *2*, 723–733.
33. Marelli, U. K.; Rechenmacher, F.; Sobahi, T. R.; Mas-Moruno, C.; Kessler, H. Tumor Targeting via Integrin Ligands. *Front. Oncol.* **2013**, *3*, 222.
34. Zhang, Y.; Hong, G.; He, W.; Zhou, K.; Yang, K.; Li, F.; Chen, G.; Liu, Z.; Dai, H.; Wang, Q. Biodistribution, Pharmacokinetics and Toxicology of Ag2s Near-Infrared Quantum Dots in Mice. *Biomaterials* **2013**, *34*, 3639–3646.
35. Bartczak, D.; Kanaras, A. G. Preparation of Peptide-Functionalized Gold Nanoparticles Using One Pot EDC/Sulfo-NHS Coupling. *Langmuir* **2011**, *27*, 10119–10123.